Combined Sidelobe Reduction and Omnidirectional Linearization of Phased Array by Using Tapered Power Amplifier Biasing and Digital Predistortion

Nuutti Tervo, *Graduate Student Member, IEEE*, Bilal Khan, *Graduate Student Member, IEEE*, Janne P. Aikio, Olli Kursu, Markku Jokinen, Marko E. Leinonen, *Member, IEEE*, Marko Sonkki, *Senior Member, IEEE*, Timo Rahkonen, *Member, IEEE*, and Aarno Pärssinen, *Senior Member, IEEE*

***Abstract*— Power amplifier (PA) efficiency and linearity are among the key drivers to reduce energy consumption while enabling high data rates in the fifth-generation (5G) millimeter-wave phased array transmitters. Analog per-branch phase and amplitude control is used to steer the beam, suppress the sidelobes, and form zeros to the desired spatial directions. The amplitude control of individual PA inputs makes nonlinearity vary from antenna to antenna, which challenges the common digital predistortion (DPD) used to linearize the array. In this article, we implement an amplitude control for beamforming by tuning the PA gate bias. Varying the output powers via PA biasing makes the nonlinear characteristics observed at the individual PA outputs similar that helps the array DPD to linearize also individual PAs. The technique is validated by both simulations and measurements. As a measurement platform, we use a 28-GHz phased array transceiver equipped with 64 antenna elements and 16 radio frequency chains. The desired beam shape is synthesized by controlling the per-antenna over-the-air-power with PA gate bias. Then, the system is linearized by training DPD with a reference antenna. The DPD is demonstrated with 100-MHz-wide 5G new radio modulated waveform. The best example case showed −23.5-dB maximum sidelobe level (SLL) with 4.9% error vector magnitude and −40.8-dB total radiated adjacent channel power ratio with DPD. The proposed approach enables simultaneous reduction of beam pattern SLL, achieves good linearity in all directions, and maintains the PA efficiency.**

***Index Terms*— Amplitude tapering, antenna array, array biasing, array calibration, digital predistortion (DPD), fifth generation (5G), linearization, nonlinearity, phased array.**

I. Introduction

MILLIMETER-WAVE (mmW) transceivers (TRXs) equipped with large antenna arrays have become the mainstream of wireless research in academia and industry. First mmW systems are already on the market and a practical breakthrough is expected in the second phase of the fifth-generation (5G) systems in the near future. In sixth-generation (6G) systems, the role of mmW is envisioned to grow even further [1]. The mmW TRXs are usually implemented as phased arrays where beamforming is mostly done in the radio frequency (RF) domain. Analog signal division to multiple parallel nonlinear RF branches challenges the standard linearization methods such as digital predistortion (DPD), which has been heavily used to linearize power amplifiers (PAs) in sub-6-GHz systems [2]–[4]. Furthermore, RF beamforming is not only done by adjusting phases but also amplitudes of the individual TRX branches that are controlled in order to form zeros and suppress the sidelobe level (SLL) [5]. In practice, the control is applied before the PA to avoid the post-PA losses that deteriorate the overall efficiency. This makes the common linearization of multiple transmitter (TX) branches challenging with a single DPD linearizer due to the fact that the PAs have different nonlinear responses. Over-the-air (OTA) combination of the nonlinearities makes the DPD performance dependent on the transmission direction [3].

The third generation partnership project (3GPP) has standardized several mmW bands for the 5G new radio (NR) cellular communications. Many of the specifications related to PA nonlinearity, such as adjacent channel power ratio (ACPR) and error vector magnitude (EVM), have already been specified, and the existing specifications [6] offer relaxed ACPR compared with the lower frequency systems. The RF performance metrics related to the mmW TRXs are specified by OTA measurements. EVM is measured in the intended beamforming direction, while ACPR is specified as total radiated power (TRP). These aspects have a significant impact on the linearization strategy if the DPD is tailored to improve the specifications used in conformance testing [7].

Phased array linearization by DPD has been studied extensively in recent literature. In most of the papers, the array is linearized in the far field by using different feedback strategies and DPD methods. Feedback is taken either from the PA outputs by switchable feedback (see [2], [5], [8]) or from an OTA reference antenna that is placed in the near field (see [9], [10]) or far field (see [3], [4], [11]–[15]). Some papers even consider weighting the feedback paths to emulate the

Manuscript received April 1, 2021; revised May 12, 2021; accepted May 22, 2021. Date of publication July 8, 2021; date of current version September 2, 2021. This work was supported in part by the Academy of Finland 6Genesis Flagship through the Business Finland 5G-VIIMA Project under Grant 318927 and in part by the Infotech Oulu Doctoral Programme. *(Corresponding author: Nuutti Tervo.)*

The authors are with the Faculty of Information Technology and Electrical Engineering (ITEE), University of Oulu, 90570 Oulu, Finland (e-mail: nuutti.tervo@oulu.fi).

Color versions of one or more figures in this article are available at https://doi.org/10.1109/TMTT.2021.3092357.

Digital Object Identifier 10.1109/TMTT.2021.3092357

array far-field conductively, as in [16] and [17]. The DPD object contains single direction (see [3], [5], [12], [13]) or the object is generated simultaneously for multiple directions, as, e.g., in [2] and [4]. The detailed review of different feedback receiver (RX) options and array DPD approaches can be found from, e.g., [18].

Different ways of generating the DPD object have their own benefits that depend on the device under test (DUT). If the parallel TX branches have differences in their nonlinear behavior, the beam of the distortion may differ from the linear part of the beam [3], [16]. When DPD is applied for the array, the distortion can be shaped to create a notch in the beamforming angle in order to boost the linearity to the direction of the RX [3], [5]. The differences in the nonlinearity may come from the intended amplitude control [5], gain variation of the phase shifters (PSs) [4], [16], [19], and/or antenna coupling [4], [20]–[22]. The drawback of the directive linearization is that the 5GNR ACPR is specified in terms of TRP, and hence, the directive linearization mostly helps to meet the EVM targets with limited total radiated ACPR (TRACPR) performance [16]. In [23], the main-lobe linearization was observed to be good also for the TRACPR reduction. However, the case study included a commercial measurement platform where only phase was controlled, and thus, the PAs were rather similar across the array. In [24], the distortion at each antenna is made more similar by using first analog predistortion for individual PAs and then linearizing the overall array with DPD. Even though the PAs were having differences in [24], the system was studied only at the outputs of two parallel PAs without having major amplitude differences among their inputs. In [22], the PAs are tuned by purposely made coupling network in the PA inputs to make the PAs more similar in order to achieve good linearization performance in all directions. The aim of the coupling network is to introduce similar nonlinearity over the nonlinear branches when multiple parallel PA outputs can be linearized by a single DPD. Hesami *et al.* [25] compromised the tapered phased array linearization performance by minimizing the maximum joint error of the individual PAs and the array.

Papers showing experimental results on array DPD use phased array implementations where only the phase of the transmit paths is purposely controlled for beamforming [see Fig. 1(a)]. Even though the works [4], [12] use a commercial phased array capable of controlling the amplitude by Cartesian PSs, they use the DUT only to control the phase (i.e., steer the beam). The impact of prior-PA amplitude control used for sidelobe reduction has been studied by simulations, e.g., in [5] and [26]. DPD measurement results in the input amplitude tapering case are studied in [25] by emulating the array with a multichannel oscilloscope. However, these papers use a traditional analog beamforming approach where the amplitude control is done prior to the similarly biased PAs. This selection makes it challenging to linearize the array in terms of TRACPR and achieve good EVM simultaneously. Hence, the approach leads to a tradeoff between directive and omnidirectional linearization performance [16], [25]. Furthermore, amplitude control implemented prior to the PA potentially

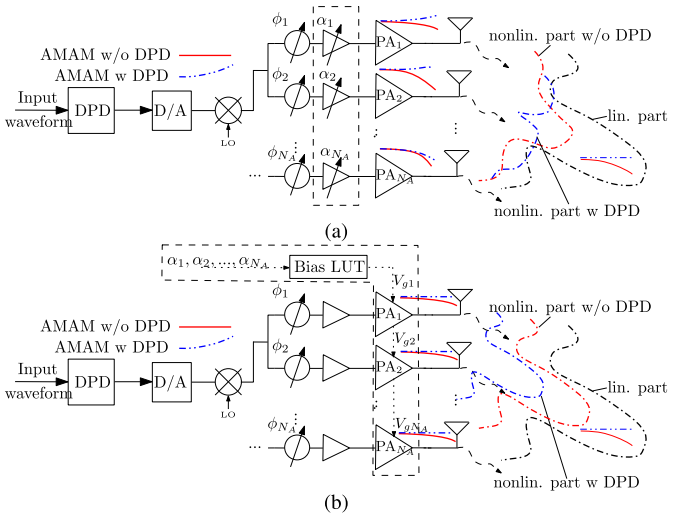

Fig. 1. Principle of the radiated distortion together with array linearization in tapered phased array that has (a) traditional analog amplitude control and (b) PA-biasing-based amplitude control. Bias control aims for similar AMAM shape across the individual PA outputs that help the DPD to linearize array in all spatial directions.

reduces the TX efficiency as some PAs may be driven with very large power backoff.

In this article, we present an alternative approach for per-branch amplitude control combined with OTA DPD for RF beamforming array [see Fig. 1(b)]. The branch-specific amplitude control is done by adjusting the PA gate bias based on OTA-calibrated bias lookup tables (LUTs). By adjusting the amplitude directly in the PA output, we can allow better efficiency from the lower power PAs in amplitude tapering. The benefit for the DPD is that the nonlinear contribution to the overall beam has a similar shape compared to the higher driven PA outputs when the proposed method is applied. The DPD and sidelobe reduction performances are analyzed in terms of SLL, EVM, main-lobe ACPR, TRACPR, and PA efficiency. The measurement results are shown for individual PA outputs and in the array far field in different directions.

The rest of this article is structured as follows. Section II introduces the concept of radiated nonlinearity and total radiated distortion. The gate-bias-based sidelobe reduction scheme together with simulation models and array DPD is shown in Section III. Section IV describes the 28-GHz phased array TX used as a demonstration platform and the PA biasing for amplitude tapering. The sidelobe reduction performance and spatial distortion behavior is measured with and without the proposed tapering scheme. Finally, a common DPD is applied for the array in Section V together with the OTA-measured sidelobe reduction, linearity, and efficiency analysis. The conclusions are drawn in Section VI.

II. Radiated Distortion From TX Array

A. Beamformed Distortion

Antenna array nonlinearity in beamforming TXs is discussed in many papers [27]–[31]. Some works [29], [30] consider that the spreading of distortion takes place mostly

in multibeam TXs where each PA is fed with a sum of multiple independent signals. Especially, Larsson and Van Der Perre [30] discussed that the antenna array transmitting only a single beam has the same nonlinear characteristics at the single PA output and at the radiated far field. However, this is not true if the nonlinear branches have differences in their nonlinear characteristics due to beamforming [5], prior-PA amplitude differences [16], PA differences [3], [17], or impedance pulling from neighboring PAs and antennas [20], [27]. Naturally, in such scenarios, the distortion may have different beams compared to the linear signal. In [31], the analysis of amplitude dependence is corrected for the multibeam scenario. However, the impact of differences in nonlinearity over the antenna branches for single-beam scenario is not considered.

In order to show that the individual PAs can have different nonlinearities compared to the radiated far-field signal, we use a simple mathematical example. Let us consider a system model shown in Fig. 1(a) without DPD. Let the array input waveform be $x(n)$, where n denotes the time-domain sample index. By modeling the signals as complex envelopes, we can write the signal in the ith PA input as

$$x_i(n) = w_i(n)x(n) \tag{1}$$

where $w_i(n)$ denotes the beamforming coefficient of the ith transmit path. The beamforming is done in both phase and amplitude. By assuming that the beamformer is the same for all time-domain samples, the coefficients can be written as

$$w_i(n) = a_i(n)e^{j\varphi_i(n)} = a_i e^{j\varphi_i} \tag{2}$$

where a and φ present the amplitude and phase of the beamforming coefficients, respectively, and j is the imaginary unit of a complex number. Now, let us model the PAs with a memoryless third-order polynomial when the output signal of the ith PA can be written as

$$\begin{aligned} y_i(n) &= K_{i,1}x_i(n) + K_{i,3}|x_i(n)|^2 x_i(n) \\ &= K_{i,1}a_i e^{j\varphi_i}x(n) + K_{i,3}|a_i x(n)|^2 a_i e^{j\varphi_i}x(n) \end{aligned} \tag{3}$$

where $K_{i,1}$ and $K_{i,3}$ denote the first- and third-order coefficients of the ith PA, respectively. The first term in (3) represents the linear part of the signal and the second term denotes the nonlinear part.

The phase and amplitude window of the linear components in the antenna branches can be expressed as

$$\vec{y}_{\text{lin}}(n) = \begin{pmatrix} K_{1,1}a_1\ e^{j\varphi_1} \\ K_{2,1}a_2\ e^{j\varphi_2} \\ \vdots \\ K_{N_A,1}a_{N_A}e^{j\varphi_{N_A}} \end{pmatrix} x(n) \tag{4}$$

where N_A denotes the number of antennas. Similarly, the phase and amplitude window of the nonlinear components over the antenna branches are written as

$$\vec{y}_{\text{nlin}}(n) = \begin{pmatrix} K_{1,3}|a_1\ x(n)|^2\ a_1\ e^{j\varphi_1} \\ K_{2,3}|a_2\ x(n)|^2\ a_2\ e^{j\varphi_2} \\ \vdots \\ K_{N_A,3}|a_{N_A}x(n)|^2\ a_{N_A}e^{j\varphi_{N_A}} \end{pmatrix} x(n). \tag{5}$$

The beam pattern of the distorted signal can be derived based on the antenna inputs. Let us assume a uniform linear array (ULA) with omnidirectional antenna elements spaced with d. The beam pattern of the antenna array can be derived as

$$F_{\text{A}}(\phi) = \vec{w}^T \vec{H}(\phi) \tag{6}$$

where $\vec{w}^T \in \mathbb{C}^{N_A \times 1}$ denotes the signals observed at each antenna element and $\vec{H}(\phi)$ denotes the complex coefficients (phase and amplitude) of the antenna array elements in each azimuth direction ϕ. $\vec{H}(\phi)$ can be written as

$$\vec{H}(\phi) = [e^{k(\phi)r_1}, e^{k(\phi)r_2}, \ldots e^{k(\phi)r_{N_A}}]^T \tag{7}$$

where r_i denotes the position of the ith antenna of the ULA, $k(\phi) = (2\pi/\lambda)\sin(\phi)$ is the wave vector with respect to the axis of the ULA, and λ is the wavelength. Hence, the beam of the linear part can be derived as

$$F_{\text{lin}}(\phi, n) = \vec{y}_{\text{lin}}^T(n)\vec{H}(\phi) \tag{8}$$

and the beam of the nonlinear part as

$$F_{\text{nlin}}(\phi, n) = \vec{y}_{\text{nlin}}^T(n)\vec{H}(\phi). \tag{9}$$

The combined beam of the signal and distortion is calculated as

$$F(\phi, n) = F_{\text{lin}}(\phi, n) + F_{\text{nlin}}(\phi, n). \tag{10}$$

In order to have different beams for the distortion than for the linear signal, we should have $\vec{y}_{\text{lin}} \neq \alpha\vec{y}_{\text{nlin}}$, where $\alpha \in \mathbb{C}$ is a scaling factor. By using (4) and (5) we can write the dependence between the linear and nonlinear components as

$$\begin{aligned} \vec{y}_{\text{nlin}}(n) &= \begin{pmatrix} \frac{K_{1,3}}{K_{1,1}}K_{1,1}a_1\ e^{j\varphi_1}|a_1\ x(n)|^2 \\ \frac{K_{2,3}}{K_{2,1}}K_{2,1}a_2\ e^{j\varphi_2}|a_2\ x(n)|^2 \\ \vdots \\ \frac{K_{N_A,3}}{K_{N_A,1}}K_{N_A,1}a_{N_A}e^{j\varphi_{N_A}}|a_{N_A}x(n)|^2 \end{pmatrix} x(n) \\ &= \begin{pmatrix} \frac{K_{1,3}}{K_{1,1}}|a_1|^2|x(n)|^2 \\ \frac{K_{2,3}}{K_{2,1}}|a_2|^2|x(n)|^2 \\ \vdots \\ \frac{K_{N_A,3}}{K_{N_A,1}}|a_{N_A}|^2|x(n)|^2 \end{pmatrix} \odot \begin{pmatrix} K_{1,1}a_1\ e^{j\varphi_1} \\ K_{2,1}a_2\ e^{j\varphi_2} \\ \vdots \\ K_{N_A,1}a_{N_A}e^{j\varphi_{N_A}} \end{pmatrix} x(n) \\ &= |x(n)|^2 \underbrace{\begin{pmatrix} \frac{K_{1,3}}{K_{1,1}}|a_1|^2 \\ \frac{K_{2,3}}{K_{2,1}}|a_2|^2 \\ \vdots \\ \frac{K_{N_A,3}}{K_{N_A,1}}|a_{N_A}|^2 \end{pmatrix}}_{\vec{w}_{nl}} \odot \vec{y}_{\text{lin}}(n) \\ &= |x(n)|^2 \vec{w}_{\text{nlin}} \odot \vec{y}_{\text{lin}}(n) \end{aligned} \tag{11}$$

where $\odot$ denotes the elementwise multiplication.

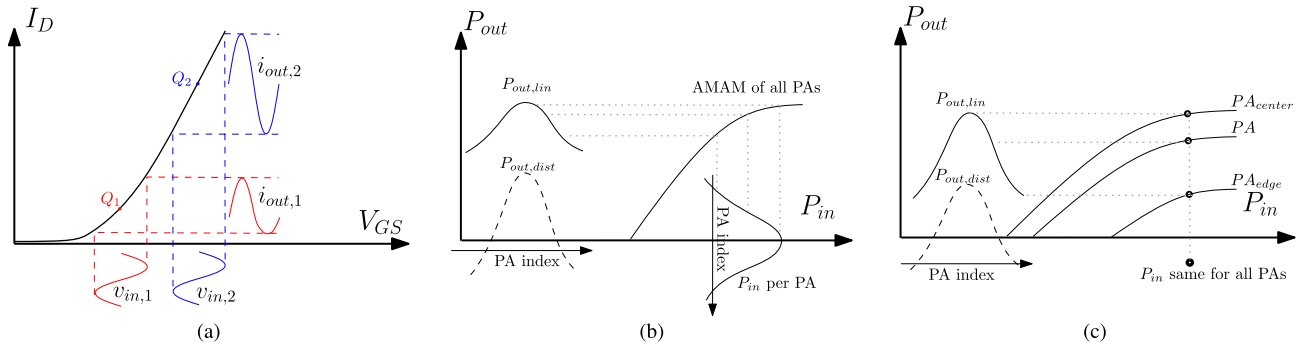

Fig. 2. (a) Generic PA biasing curve, (b) principle of per-antenna power control of equally biased PAs, and (c) per-antenna power control via PA gate bias. PA index in the figures denotes the individual PAs of the array in amplitude tapering case.

Special case for array with only phase control and equal PAs, i.e., $a_i = 1$ and $K_{il} = K_l$, where l denotes the order of the nonlinearity, gives $y_{\text{nlin}}(n) = (K_3/K_1)|x(n)|^2\vec{y}_{\text{lin}}(n)$. In such a case, the beam of the distortion is a scaled version of the beam of the linear signal, i.e., their spatial shape is the same. However, in practice, the amplitude is desired to be controlled, which causes an amplitude window for the nonlinearity. Obviously, by looking at (11), we see that if the window of the nonlinearity $\vec{w}_{\text{nlin}}$ is not unitary, i.e., $\vec{w}_{\text{nlin}} \neq \alpha\vec{1}$, the beam of the distortion is different from the linear part of the beam. This means that linearizing an individual PA or linearizing a single direction does not provide uniformly distributed linearization.

B. Total Radiated Distortion and Array Efficiency

To address the possibility for different spatial distributions of distortion, 5GNR [7] specifies out-of-band distortion in terms of TRACPR that is integrated over the space. With array DPD, this has been considered, e.g., in [16], [18], and [23]. By using the polynomial approach presented in Section II-A, the total radiated linear power over the azimuth plane can be calculated as

$$P_{\text{lin,TRP}} \approx \frac{\pi}{2N_{\text{az}}} \sum_{m=0}^{N_{\text{az}}-1} P_{\text{lin}}(\phi_m) \tag{12}$$

where ϕ denote the azimuth angles with discrete grid over N_{az} values and

$$P_{\text{lin}}(\phi_m) = \frac{1}{N_{\text{s}}} \sqrt{\sum_{n=0}^{N_{\text{s}}-1} |F_{\text{lin}}(\phi, n)|^2} \tag{13}$$

is the root-mean-square (rms) power calculated across the N_s time-domain samples. Similarly, the total radiated nonlinearity over the azimuth domain can be written as

$$P_{\text{nlin,TRP}} \approx \frac{\pi}{2N_{\text{az}}} \sum_{m=0}^{N_{\text{az}}-1} P_{\text{nlin}}(\phi_m) \tag{14}$$

where

$$P_{\text{nlin}}(\phi_m) = \frac{1}{N_{\text{s}}} \sqrt{\sum_{n=0}^{N_{\text{s}}-1} |F_{\text{nlin}}(\phi, n)|^2}. \tag{15}$$

The fraction $P_{\text{nlin,TRP}}/P_{\text{lin,TRP}}$ describes the total radiated nonlinearity and has similar meaning than total normalized mean square error (NMSE) or TRACPR. The main-lobe linearity can be calculated as $P_{\text{nlin}}(\phi_{\text{s}})/P_{\text{lin}}(\phi_{\text{s}})$, where ϕ_{s} is the steering angle.

Also, power efficiency of the array can be defined based on the radiated powers. In this article, we use two figures of merit to describe the array power efficiency. The first one is

$$\eta_{\text{EIRP}} = \frac{\text{EIRP}}{P_{\text{dc}}} \tag{16}$$

where EIRP is the effective isotropic radiated power and P_{dc} denotes the sum direct current (dc) power consumption over the PAs. Similarly, the TRP efficiency is calculated as

$$\eta_{\text{TRP}} = \frac{P_{\text{TRP}}}{P_{\text{dc}}} \tag{17}$$

where P_{TRP} is the TRP calculated similar to (12).

III. Sidelobe Reduction in Phased Array TXs With Nonlinear PAs

In this section, we describe and evaluate two alternative amplitude control approaches for analog beamforming TX. The principles can be explained by using the traditional PA biasing curve shown in Fig. 2(a). In the first scenario, we bias the transistor to a fixed operation point and vary the input amplitude. In power domain, the scenario is shown in Fig. 2(b). The AMAM behavior of the PAs is similar, but they are driven with different power levels as noted in the power distribution over the PAs in the figure. Therefore, the center PAs are distorting more than the PAs at the edge of the array. This means that the distortion experiences vary different distribution over antennas and has different beam than the linear signal. In the second scenario, the PAs are driven with equal input amplitude, while the output current, and hence output power, is directly controlled by varying the PA gate voltages. In the power domain, the scenario is shown in Fig. 2(c). All PAs are driven with equal input power and the bias control is used to decrease the gain and compression point of the lower driven PAs. Therefore, all PAs are distorting the signal at the PA outputs. The objective is simultaneous amplitude tapering as well as to equalize the shape of the nonlinearity across the PAs

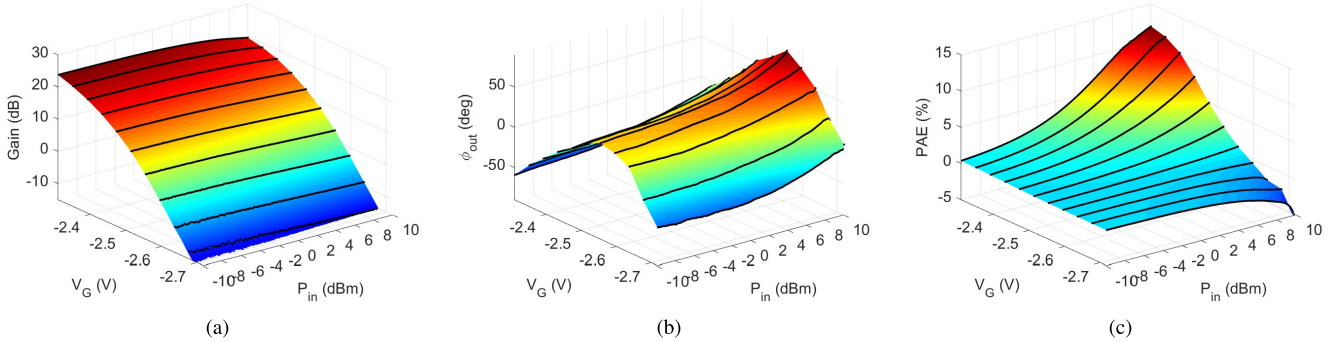

Fig. 3. (a) Gain, (b) AMPM, and (c) PAE versus P_{in} and V_G LUT-models generated from the CW measurements of a single transmit path. The black points in the figures represent the original measurement data and the colored areas show the interpolated values.

that lead to a similar spatial shape of the linear signal and distortion. In the following, the techniques and their impact on the array nonlinearity are explained by using a simulation example.

A. Experimental Bias-Dependent LUT PA Model

Physical PA model that includes realistic impacts of both amplitude control schemes together with nonlinear amplitude, phase, current, and efficiency behaviors is challenging and art on its own. Especially, when it comes to beamforming and nonlinearity, we need to observe the nonlinear impacts over all antennas, i.e., over space, and also over the waveform samples, i.e., array input power. For beamforming, the main objective is in the mean of the signal, whereas for distortion, the peaks with varying envelope communication signals play the main role. Both of these need to be included in the simulation model to gain realistic results. Hence, for modeling of a gallium nitride (GaN) mmW PA used in the experiments of this article, we used a multidimensional LUT that is derived based on an extensive measurement campaign of a 28-GHz phased array TX [32]. The array is the same as used, e.g., in [18]. The measurements are performed for a single PA branch OTA in two stages by using a second TRX unit as a reference mixer similarly as in [33]. In the first set of measurements, we performed a continuous-wave (CW) power sweep at 28.1 GHz for different gate voltage values from -3 up to -2.35 V. In the second-stage measurement, the power is swept manually in order to capture how much dc power the PA is drawn from the supply. This is done in order to get a realistic power efficiency model for the simulations. Using CW signals enable phase coherency between measurements performed in different time instants that are crucial to capture the impact of bias control on the output signal phase. The derived LUT modeling enables to simulate the PAs in different power levels and bias voltages that are crucial for both of the studied amplitude tapering schemes.

1) Impact of PA Biasing on AMAM: The measured gain of the transmit path as a function of input power and V_G is shown in Fig. 3(a). The black points in the figure correspond to the actual measurement data, while the colored areas are interpolated values. Clearly, varying V_G has a direct impact on the PA gain and, hence, the output power. With very low V_G values, the behavior of the PA is slightly expansive with

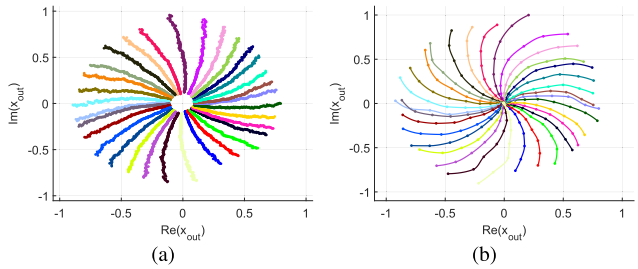

Fig. 4. Measured AMAMs and AMPMs presented as an IQ-map with different PS values for (a) varying input power and (b) varying PA bias point. Different colors show the behavior with different PS states.

low signal levels and the compression starts earlier due to the fact that the PA is biased toward more nonlinear PA classes, such as classes B and C (see Fig. 2). When V_G is increased toward class AB, the output is compressed earlier, and hence, even with lower output powers, the PA is nonlinear. When biased toward class A, the gain is higher, and hence, also the output compression point is increased. As a result, by choosing proper bias points, we can control the PA gains and vary the amplitude of individual transmit paths for sidelobe reduction, as shown in Fig. 2.

2) Impact of PA Biasing on AMPM: The measured amplitude modulation-to-phase modulation (AMPM) behavior of the transmit path with different gate voltages as a function of input power is shown in Fig. 3(b). The AMPM versus the input power is expansive. However, when increasing the gate bias, the phase is first increasing and then decreasing as the PA moves toward more linear operation point. Therefore, when controlling the gate bias, the impact can be observed not only in the gain but also in the varying output phase. The main reason for the transistor nonlinear AMPM behavior is usually the signal-dependent input capacitance that pulls the input matching and causes phase shift at the transistor input [34]. Similarly, varying the PA gate voltage changes the input capacitance and hence has a direct impact on the signal mean phase as well as the nonlinear AMPM. In the literature, this has also been observed in GaN devices such as in [35].

Orthogonal phase and amplitude control are useful for maintaining independent control of beam steering and sidelobe suppression [36]. Due to the nonlinear AMPM, the control is not directly orthogonal. This can be observed in Fig. 4, where

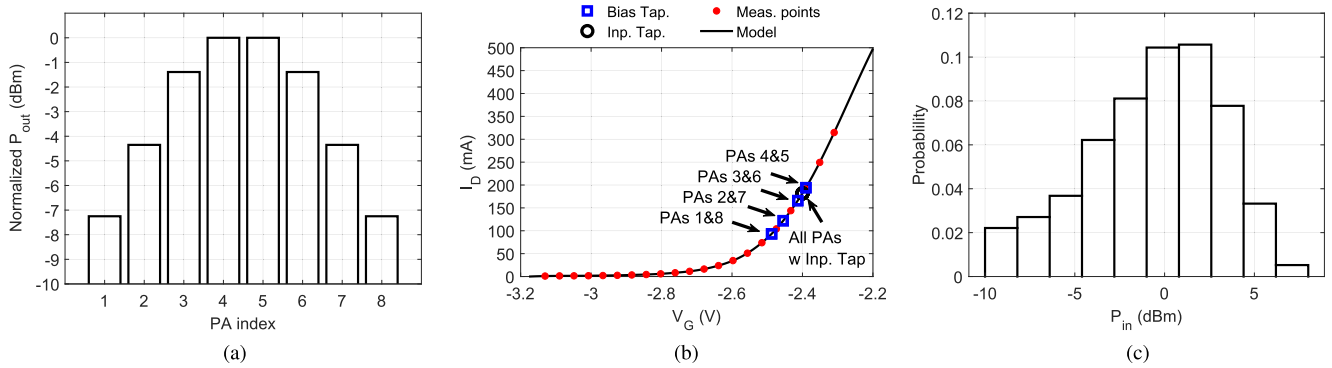

Fig. 5. (a) Required output powers per PA for 24-dB Taylor tapering. (b) GaN PA I_D versus V_G with selected bias points. (c) Input power distribution of the waveform for array simulations.

the phase and amplitude measurements are performed with 32 different PS values with both amplitude control schemes and observed in the in-phase and quadrature-phase (IQ) plane. The plots correspond to a complex-valued codebook of possible beamforming coefficients. Input power sweep with fixed bias point is shown in Fig. 4(a), and gate voltage sweep with fixed input power is presented in Fig. 4(b). For exactly orthogonal phase and amplitude control, the curves should be straight lines starting from the center and going toward the endpoint of the circle. With bias control, the phase varies more than with input power control. However, amplitude tapers as such are not usually varied rapidly for every steering angle as the requirement for sidelobe reduction is similar to all steering angels. Therefore, in phased arrays, the impact of PA biasing on the mean signal phase can be calibrated by the same PSs that are used for beamforming. Hence, the varying bias points have to be considered in the PS control words. Note that the same applies also for input amplitude control if the PAs are operating in the nonlinear region.

3) Efficiency With Varying Bias Points: The measured power added efficiency (PAE) with varying gate bias is shown in Fig. 3(c). Note that as these are observed by OTA measurements, the results do not necessarily correspond to a PA-only efficiency. From the figure, we can observe that the efficiency increases earlier in power when the bias is lowered. Hence, when the output power is controlled directly by PA biasing, the efficiency can be potentially increased. However, if the gain is lowered below 0 dB, the PAE becomes negative, which means that the path is attenuating. Therefore, the useful control range is obviously less than the highest gain value of the used PA, in this example around 20 dB. This is more than enough for reducing the SLL in phased arrays where usually the required control dynamics for practical tapering schemes is less than 10 dB.

B. Radiated Distortion Example With −24-dB Taylor Tapering

In this section, the measurement-based LUTs derived in Section III-A are used to evaluate the amplitude control principles and their radiated distortion performance. The LUTs are interpolated by using cubic shape-preserving piecewise interpolation. The points that are below the measured range are extrapolated by using linear extrapolation. As an example, we use a linear eight-element phased array with omnidirectional antenna elements and antenna spacing of $d = \lambda$ at $f_0 = 28.1$ GHz. The parameters for the example are chosen to correspond to the experimental validation presented in Section IV. In order to reduce the sidelobes of the beam pattern, we use the Taylor window with -24-dB SLL target over the antenna elements. The normalized power window is shown in Fig. 5(a). The window has around 7-dB dynamic range over the antenna powers. Each antenna is driven with a dedicated PA following the LUT model presented in Section III-A. The chosen bias points for the bias tapering are $V_G = -2.39, -2.41, -2.54$, and -2.49 V from largest to smallest, and for input tapering, the PAs are biased to $V_G = -2.4$ V. Note that the taper is symmetric and, hence, the other half of the PAs is having the same controls but in reverse order. The points are shown in Fig. 5(b) together with the measured I_D versus V_G.

The simulations are driven with a power sweep that has similar PAPR behavior to a traditionally modulated communication signal. The histogram of the input powers over the power sweep is shown in Fig. 5(c). The input distribution is truncated to limit the powers that go significantly outside the measured LUT. The results are evaluated in the individual PA outputs by using AMAM, AMPM, and PAE and over the azimuth angles by simulating the beams of the individual nonlinear coefficients of the transmit paths.

1) Nonlinear Behavior at the PA Outputs: The simulated AMAM, AMPM, and PAEs with both tapering schemes are shown in Fig. 6(a)–(c). For input tapering, the input powers are varied such that the outputs of the PAs achieve the target power distribution as, otherwise, the sidelobe reduction performance would be reduced as it has been shown in [5]. With input power tapering, the PAs with higher input power compress more than the ones with lower input power. The output power calibration increases the dynamics over the PA inputs even more as the center PAs are compressing more than the PAs that have lower input amplitude. In the bias tapering case, each AMAM curve is similarly compressing. AMPMs of PAs are shown in Fig. 6(b). A similar observation can be made compared to the AMAM case; the shape of the AMPM in case of bias tapering is more similar across all PAs, while for input

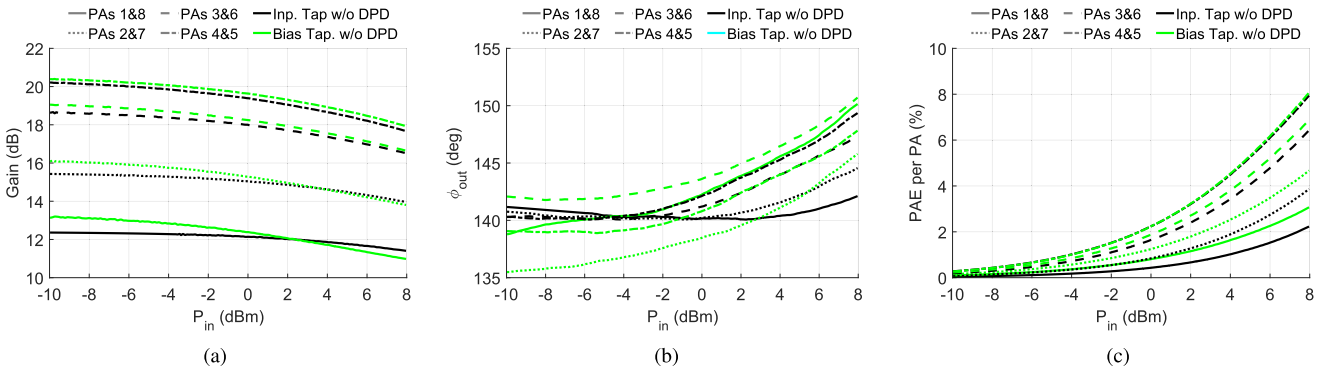

Fig. 6. Simulated (a) AMAM, (b) AMPM, and (c) PAEs of the PAs with both tapering schemes in an eight-antenna array, where indices 4 and 5 are in the center. Different line types are the results for different PAs, while black and green colors are the results for input tapering and bias tapering schemes, respectively.

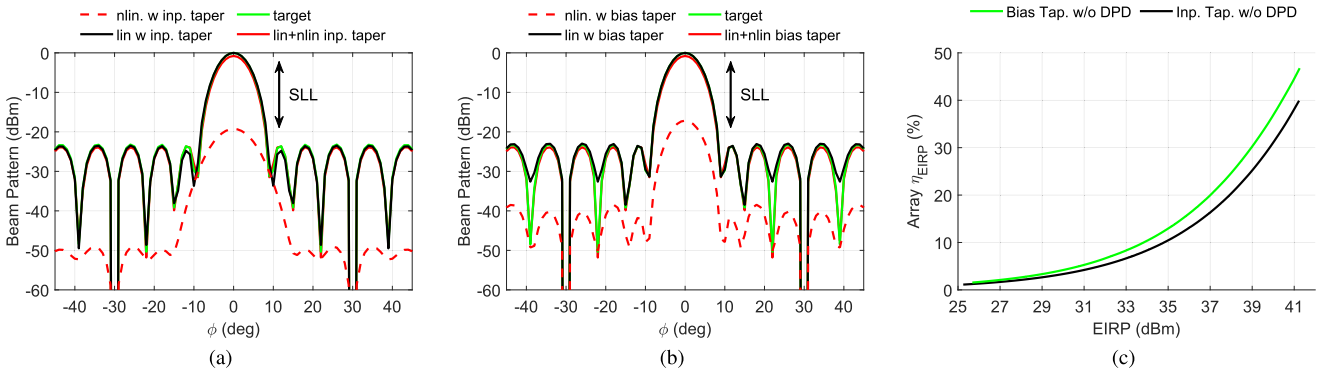

Fig. 7. Simulated beam patterns of linear and nonlinear parts with (a) input amplitude tapering with fixed bias point, (b) bias tapering with fixed input amplitude, and (c) overall array efficiency with both tapering schemes.

tapering case, the AMPMs of the PAs with different output powers differ from each other. However, with bias tapering, the mean level of the whole AMPM curve varies from PA to PA as expected. The results shown in the figure have already 5-bit phase calibration included. The PS states of the PAs with the lowest power levels (PAs 1, 2, 7, and 8) are increased by one state, i.e., 11.25° according to Fig. 4(b).

PAEs of both tapering schemes are shown in Fig. 6(c). In both tapering scenarios, the PAs with the highest output power have the same PAE as they are biased nearly to the same operation point. As expected, the PAEs of the PAs with lower output power are increased by bias tapering compared with the input amplitude tapering. The improved efficiency is achieved by lower bias current that drives the PA toward more efficient but also more nonlinear power classes. However, the observed mean PAEs under backoff are still rather small.

2) Sidelobe Reduction and Radiated Distortion: The beam patterns of the fundamental signal and distortion with both tapering schemes are derived as follows. First, we fit a fifth-order polynomial to each PA output by using the least-squares (LS) estimation. By doing this, we can observe the beam of the linear and nonlinear parts of the signal derived in Section II-A. Note that the polynomials are fit between the common input signal and the output of each PA individually, and hence, the operation point after the fitting is fixed. The beams of linear and nonlinear parts are derived by using (8) and (9). Also, their sum calculated as (10) is derived to present the overall beam pattern. The simulation results are shown in Fig. 7(a) and (b) for input tapering and bias tapering scenarios, respectively. All beams are normalized by the maximum of the linear part in order to make comparison easier and also to see the amount of distortion radiated in each direction. The overall beam pattern is slightly below the beam of the linear part due to the compression caused by the nonlinearity. The SLLs are calculated based on the overall beam. The tapered beams have an average SLL of -23.4 dB in the input tapering case and -22.9 dB in the bias tapering case. The slight difference in sidelobe reduction performance is due to the AMPM behavior that cannot be fully corrected by the used 5-bit PSs. In the input tapering scenario, the shape of the beam patterns of linear and nonlinear parts is very different due to the fact that the center PAs dominate the nonlinearity. In fact, the nonlinearity has clearly less directivity compared to the linear part. This is due to the fact that only the center PAs have a significant amount of nonlinearity. A similar observation for input tapering case has been made in [5]. On the contrary, with bias tapering scheme, PAs were observed to be more similar. This is clearly seen in the beam shape of the distortion in Fig. 7(b). Due to the fact that all PAs contributed to the overall nonlinearity, the distortion level is slightly increased in the main lobe compared to the input tapering scenario.

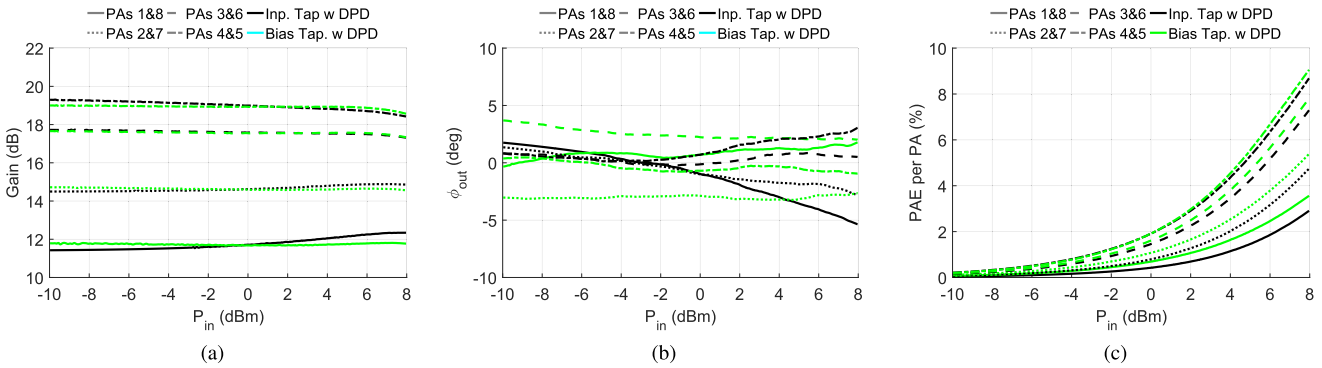

Fig. 8. Simulated (a) AMAM, (b) AMPM, and c) PAEs of the PAs with both tapering schemes and array DPD. Different line types are the results for different PAs, while black and green colors are the results for input tapering and bias tapering schemes, respectively.

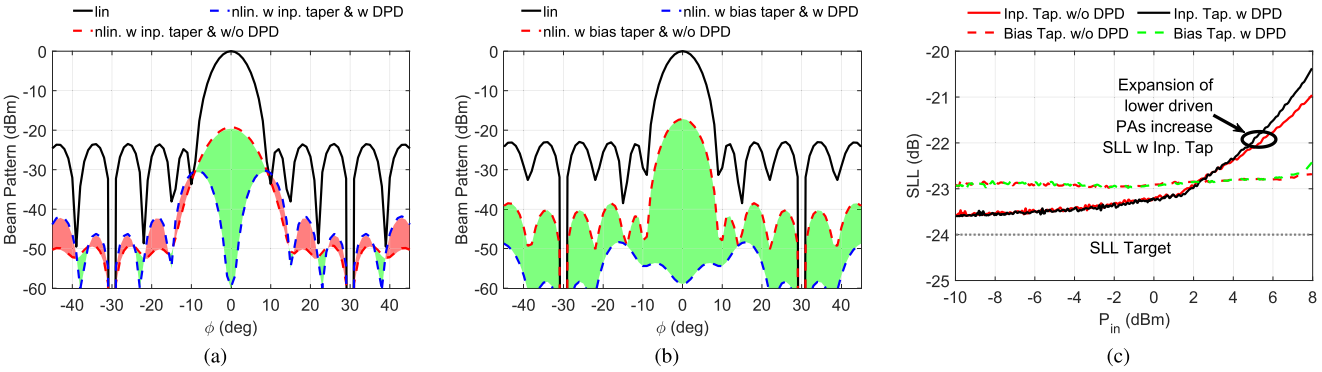

Fig. 9. Simulated beam patterns of linear and nonlinear parts with DPD in (a) input amplitude scenario tapering with fixed bias point, (b) bias tapering scenario with fixed input amplitude, and (c) SLL versus P_{in} in both tapering scenarios with and without DPD. In the beam figures, the green/red areas indicate the linearity improvement/deterioration in different directions caused by main-lobe DPD.

The overall nonlinearity can be evaluated by two FOMs defined in Section II-B that are the fraction between the linear and nonlinear parts in the main lobe and the total radiated distortion integrated over the space. The fraction has a similar meaning than, for example, signal-to-distortion ratio (SDR) or NMSE when modulated signals are used. Also, it is highly related to ACPR, which is usually a bit lower than NMSE in the memoryless case. The results are also collected in Table I. For the input tapering case, the main-lobe nonlinearity is -19.1 dB, whereas for the bias tapering case, it is -17.1 dB. The corresponding total radiated nonlinearities are -18.5 and -18.8 dB. Hence, even though the nonlinearity in input tapering case is slightly lower in the main lobe, the total nonlinearity is almost the same compared to the bias tapering scenario. The results indicate that with the chosen input parameters, tapering through the PA biases may increase the main-lobe distortion, but the beam of the nonlinearity can be more similar compared to the linear beam. Hence, bias control makes it possible to have an impact on the beam of the radiated nonlinearity.

C. Impact of Main-Lobe Linearization by DPD

When PAs have different nonlinear characteristics, per-PA linearization is challenging. However, the beam can be linearized in the main lobe as done, e.g., in [5]. In this section, we use a common DPD to linearize the main lobe for the two amplitude tapering examples presented in Section III-B. The used DPD is a simple memoryless fifth-order polynomial and the coefficients are solved based on LS fitting. The array simulations are then run through again with DPD and LUT PA models. For observing the linearized beams, new coefficients are fit based on the linearized output and raw input.

The simulated AMAMs and AMPMs with DPD are shown in Fig. 8(a) and (b). As expected, in case of input amplitude tapering, the lower driven PAs are expanding, while PAs with higher output power are still slightly compressing even with DPD. This can be clearly observed in the beam pattern that is given in Fig. 9(a). In the figure, the green and red areas indicate the regions where the linearity is either improved or deteriorated, respectively. In the input tapering case, the DPD is minimizing the distortion in the beamforming angle by spreading the distortion in other directions. On the contrary, with bias tapering, AMAMs of all PAs are more linear and the lower driven PAs are not expanding. The corresponding beam pattern given in Fig. 9(b) shows that in the bias tapering scenario, the DPD is less directive, and thus, the distortion is reduced in all directions. The figures of merit are collected in Table I to ease the comparison. The total nonlinearity with DPD in the input tapering case is -31.2 dB, whereas in the bias tapering case, it is -47.9 dB. Hence, if the nonlinear responses of the PAs are more similar, we can see a clear improvement in the overall linearization performance of the

TABLE I
COMPARISON OF THE SIMULATED EIRPS, SLLS, MAIN-LOBE NONLINEARITY, TOTAL RADIATED NONLINEARITY, AND OTA EFFICIENCIES OF BOTH TAPERING SCHEMES

Scenario	EIRP (dBm)	SLL (dB)	$P_{\text{nlin}}(0)/P_{\text{lin}}(0)$ (dB)	$P_{\text{nlin,TRP}}/P_{\text{lin,TRP}}$ (dB)	η_{EIRP} (%)	η_{TRP} (%)
Input Taper w/o DPD	35.1	-23.4	-19.1	-18.5	10.6	2.3
Bias Taper w/o DPD	35.2	-22.9	-17.1	-18.8	13.7	3.0
Input Taper w DPD	34.9	-23.5	-56.8	-31.2	10.4	2.3
Bias Taper w DPD	34.9	-22.9	-55.9	-47.9	12.7	2.8

DPD. At the same time, the two techniques have nearly similar main-lobe linearity that indicates the possibility for good EVM.

Similar observations can be made based on the AMPM. With bias tapering, the AMPM is more flat for all PAs compared to the input tapering case. The impact can be illustrated by calculating the SLL with different instantaneous input power levels and the results are given in Fig. 9(c). Sidelobe reduction performance of amplitude tapering schemes is known to be sensitive to phase errors [37], [38]. As we can observe, with input amplitude tapering, the sidelobes are higher for the peaks of the signals than for the mean of the signal due to the differences in the nonlinearity among the parallel PAs. With bias tapering, PAs are more similar over the instantaneous array input power levels, which makes the SLL less dependent on the signal envelope. The nonlinearity makes the beam dependent on the waveform envelope, and hence, the beam shape varies over time. Similar AMAM and AMPM across the PAs make the SLL nearly constant for the bias tapering case, while in the input tapering case, the SLL raises for higher values of input power. While this does not have significant impact on the mean SLL (i.e., under backoff), it does spread the distortion across the space and increases the peak power in the sidelobes.

The simulated main-lobe efficiency η_{EIRP} and total drain efficiency η_{TRP} are given in Table I. Slightly better efficiency is achieved with the bias tapering scenario. Note that these results are efficiencies under 8-dB backoff from the signal peak. While the absolute efficiency improvements are minor in absolute, the relative improvement is more than 20 %. Hence, if more nonlinear PAs were used, it could be possible to achieve higher efficiency. The following will focus on the experimental validation of the PA-biasing-based amplitude tapering and its impact on the array DPD performance.

IV. GATE-BIAS-CONTROLLED RF BEAMFORMING TX AND OTA MEASUREMENT SETUP

A. 28-GHz Phased Array TRX

The demonstration platform is a 16-chain phased array TRX operating at 26.5–29.5-GHz frequency range [18], [32], [39]. In this article, we use the array at a 28.1-GHz center frequency in the TX mode. The block chart of the full TRX printed circuit board (PCB) is shown in Fig. 10. The used intermediate frequency (IF) input is at 4-GHz center frequency. The IF-to-RF path consists of bandpass filter and HMC264LC3B subharmonic mixer driven with 12.1-GHz local oscillator (LO). The MASW-011036 TRX switches (SWs) are used to

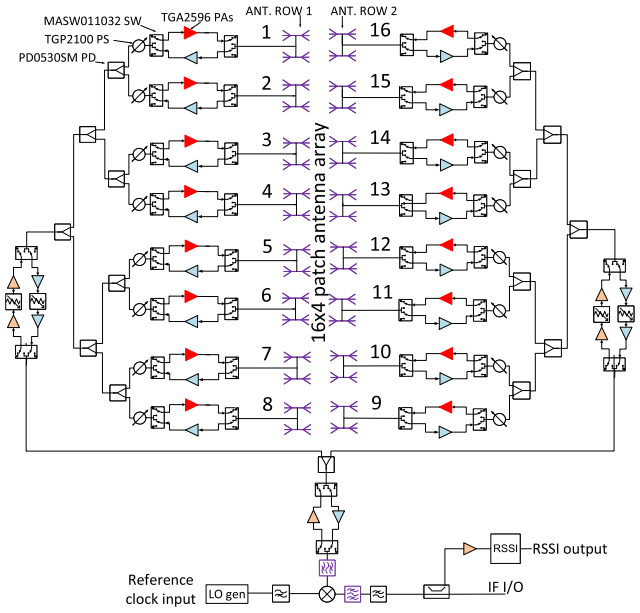

Fig. 10. Block diagram of the 28-GHz phased array TRX.

separate TX and RX paths. In the common path, we use Qorvo TGA2595 GaN PAs to amplify the signal before the first power division. After the first amplifier blocks, the signal is divided into two eight-element rows of RF branches. For both rows, we have two TGA2595 PAs separated by a controllable 5-bit HMC939 attenuator in order to ensure the stability of the TX chain. The signal is divided into parallel paths by PD-0530SM Wilkinson power dividers (PDs). Each path is equipped with TGP2100 5-bit PS and TGA2595 PA. The output of each PA is connected to a subarray, which consists of 2×2 patch antenna subarray. Each element of the subarray is fed with equal amplitude and phase. Hence, in total, the 16-chain phased array drives a 64-element antenna array configured to 16×4 formation with λ spacing between the subarrays [40] at 28 GHz. In the antenna array, the isolation between the antenna ports is better than 30 dB, and hence, coupling does not cause significant impedance pulling for the neighboring PAs. The antenna array is connected to the TRX PCB via subminiature push-on micro (SMPM)-bullets.

B. OTA Setup for Beam Measurements

A photograph of the OTA measurement setup in an anechoic chamber is shown in Fig. 11. Baseband complex-valued signal samples are generated in MATLAB and fed to Keysight M8190A arbitrary waveform generator (ARB). The ARB is

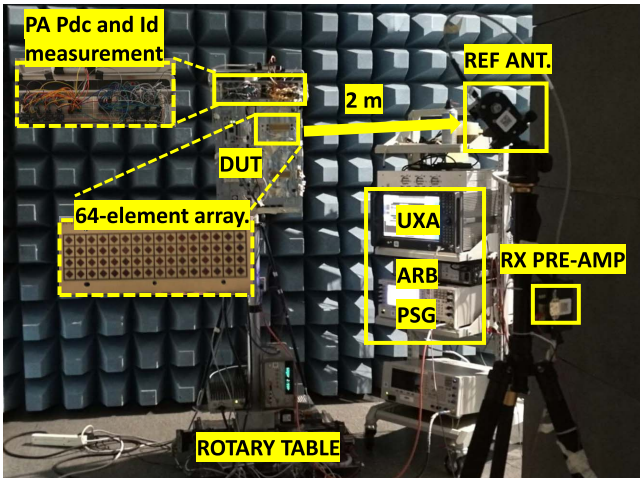

Fig. 11. Measurement arrangements in the antenna chamber.

connected to a Keysight E8257B programmable signal generator (PSG) via differential IQ ports for providing the IF input required for the DUT. The DUT has a separate control PCB for regulating the required voltages and controlling the TRX board. The controls are hosted from MATLAB via a microcontroller in order to control the LO, PSs, attenuators, TRX SWs, and PA biasing from the same measurement software. The drain current and dc power consumption of the individual PAs are measured using 16 INA219 inter-integrated circuit (I2C)-readable current sensors, two Adafruit TCA9548A 1-to-8 I2C multiplexers, and a Raspberry Pi with python code for wireless reading to MATLAB. The DUT is attached to a rotary table for the azimuth domain beam measurements with 1° angular resolution. The receive end consists of A-info LB-28-15 standard gain horn antenna placed in the DUT far field at 2-m distance and CA2630-141 preamplifier to amplify the signal for Keysight N9040B UXA signal analyzer. Vector signal analyzer (VSA) software is used to sample the signal from UXA to MATLAB and measure EVM. The DUT and all measurement equipment are controlled from MATLAB-based control software for fully automated measurements. When analyzing the results, the losses of the cables, the gain of the RX horn antenna, and the used preamplifier were separately measured and compensated from the measurements. As a waveform in all modulated signal measurements, we use a 100-MHz-wide 64-QAM cyclic prefix (CP)–orthogonal frequency-division multiplexing (OFDM) signal. The frame structure follows the 3GPP/NR standard for FR2 frequencies. The used waveform has a PAPR of 10.9 dB measured from the PSG output. Unless otherwise noted, the measurements are performed over one subframe of the signal. All the measurements are performed OTA, and hence, the PA output characteristics include also the impact of the antennas. The used FOMs describing the signal quality and beam shape are EIRP, SLL, ACPR, and EVM. Out-of-band distortion power beams are plotted as absolute adjacent channel power (ACP). The efficiencies and TRACPRs are analyzed later on in Section V.

C. PA Bias Calibration

In practical platforms, PAs are not identical. The differences can be associated with the devices themselves but also with the impedance they see in the input and output. Hence, bias (power) and phase calibration is required for every transmit path. In our platform, the PA gate voltages are controlled by LMP92066 12-bit digital-to-analog converters (DACs) operating from −5- to 0-V range. In other words, the DAC gives around 1.22-mV resolution for controlling the voltage. The DAC has two channels, and hence, one DAC controls two parallel PAs.

In order to systematically adjust the gate-bias-controlled gains (and thus the shape of the beam pattern), a similar LUT that was presented in Fig. 3 was derived for each of the transmit path. The paths are enabled one-by-one by using the time-division duplex (TDD) SWs similarly as in [18]. The complex-valued gain, i.e., S_{21}, of each path with different V_G values were measured by the reference DUT RX that dowconverted the signal back to the same IF frequency by the setup given in [33]. Hence, also the phase of each path with different bias control values was extracted from the same measurements. The calibrations are performed with the mean signal power that is used in the modulated signal measurements. Note that the used measurement platform did not allow independent input amplitude control for the PA inputs by using variable gain amplifiers or controllable attenuators. Hence, we cannot perform the measurement-based comparison of the bias control technique against the traditional amplitude control scheme that was given in Section III. In the following, we give three measurement examples where the transmit paths are calibrated to equal power and two different Taylor tapered power distributions.

1) Equal EIRP PA Calibration: As a reference case for tapering, the PA gate biases were adjusted to equalize the EIRPs measured from the far-field observation point. One should note that this does not necessarily mean that PAs would be driven with the same input power or that their nonlinear contribution to the radiated signal would be equal. This is due to the fact that there are also differences in antenna element gains. The estimated maximum variation of the antenna gains is around 4 dB from port to port, and it is highly dependent on the attached backplate [40] of the antenna and the interconnection between the RF and antenna boards.

In the untapered case, the gate voltage of each PA was selected to produce 16.5-dBm EIRP at the boresight direction. The measured EIRPs and ACPs over the PAs are shown in Fig. 12(a). The measured EIRPs are very close to the target and have less than ± 1-dB variation. The variation in ACP is around three times higher. The measured maximum ACPRs vary from 30 to 33 dB. The corresponding beams are plotted in Fig. 13(a). The measured EIRP is 39.9 dBm, EVM is 8.5%, and main-lobe ACPR is −28.9 dB. The SLLs of the channel power are −13.8 and −12.1 dB in the left and right sides, respectively. The sidelobes of the ACP are around the same although slight variation in the beam shapes of ACP and channel power can be obtained. This was expected due to the fact that the powers and nonlinearities of the individual branches are very similar to each other but still slight variation may be present.

2) Bias Tapering for −24- and −30-dB SLL: By using the same approach presented in Section III, we generated the bias

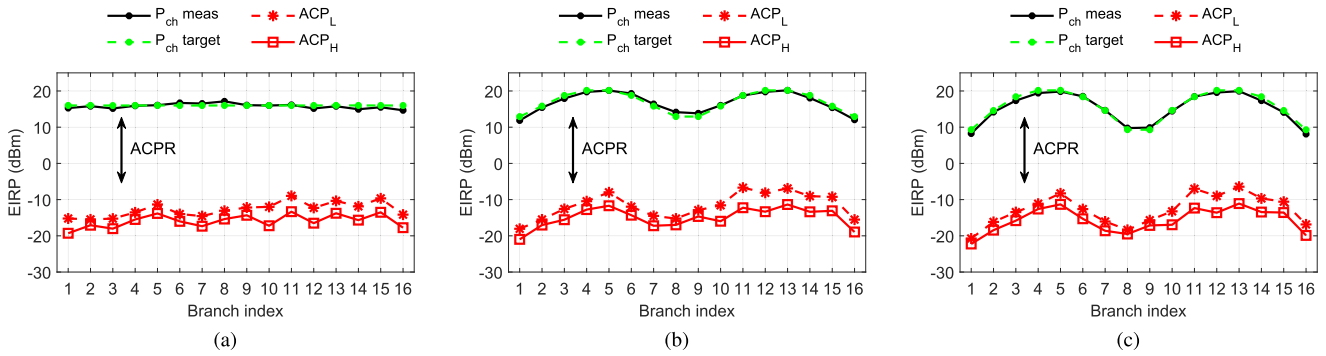

Fig. 12. OTA-measured P_{ch} and ACPs per branch for (a) uniform amplitude excitation, (b) −24-dB, and (c) −30-dB Taylor tapering PA bias calibration.

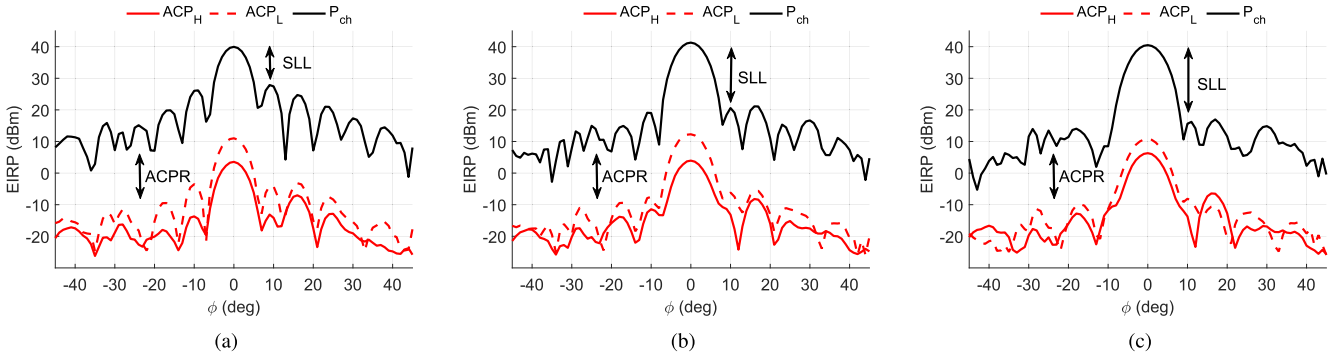

Fig. 13. OTA-measured beams of P_{ch} and ACPs for (a) uniform amplitude excitation, (b) −24-dB, and (c) −30-dB Taylor tapering PA bias calibration.

voltages for amplitude tapering. The EIRP versus gate voltage LUTs were used to generate the V_G for Taylor tapers with SLL target of −24 and −30 dB for the first four sidelobes. The same window with length of 8 was used for both of the antenna rows of our demonstration platform. Note that the phase of each branch was calibrated by separate phase measurements in order to compensate for the impact of biasing on the AMPM.

The OTA measured EIRP and ACP distributions over the PAs are shown in Fig. 12(b) and (c) for −24- and −30-dB SLL targets, respectively. The branch indexing is the same as shown in Fig. 10 such that indices 1–8 correspond to the first row and indices 9–16 correspond to the second row. As we can see, the EIRP distribution follows the target distribution well and both of the antenna rows comply with the desired tapering window. Also, the ACP distribution is very similar compared to the desired Taylor window. In Section III-B, we observed that when the tapering is performed for the inputs of similarly biased PAs, the variation in nonlinearity over the branches is more than the linear part. For the PA bias-based tapering, the nonlinear and linear parts of the signal were having a similar spatial distribution. Also, in the measured distributions of the bias taper, all PAs have a contribution to the overall nonlinearity.

The corresponding measured beam patterns of the channel power and ACPs are shown in Fig. 13(b) and (c). The measured EIRPs are 41.2 and 40.5 dBm for target SLLs of −24 and −30 dB, respectively. When decreasing the target SLL, the required output power of the PAs placed to the edge of the array is reduced, which naturally reduces the overall EIRP. The achieved SLLs are −20.2 and −26.4 dB in the right side and −22.2 and −23.5 dB in the left side. The asymmetry is caused by the beam patterns of the individual antenna elements and the phase errors of the transmit paths that cannot be fully calibrated by 5-bit PSs. The result with −24-dB SLL target is well in line with Section III-B where −22.9-dB SLL was achieved by the same target distribution. The beam patterns of the ACPs look similar compared to the beam of the channel power, but they are not identical due to the fact that there are slight differences in the nonlinearity of the individual transmit paths. Also, the frequency dependence of the antenna array behavior has an impact on the beams that are seen in particular close to the nulls. The measured main-lobe EVMs are 8.3% and 8.9% with −24- and −30-dB SLL targets, respectively.

V. Array DPD With Gate-Bias-Assisted PA Amplitude Control

As noticed in Section III-C, the beam of the nonlinearity with DPD can vary significantly from the beam of the linear part even though, without DPD, they would look very similar. In this section, we use OTA trained DPD to linearize the array with the presented bias control strategy used to reduce the sidelobes. The overall concept is shown in Fig. 14. The linearization results for individual PA outputs and radiated beams are analyzed. The results are observed for each transmit path individually and for the array to different directions by using channel power, SLL, EVM, and main-lobe ACPR.

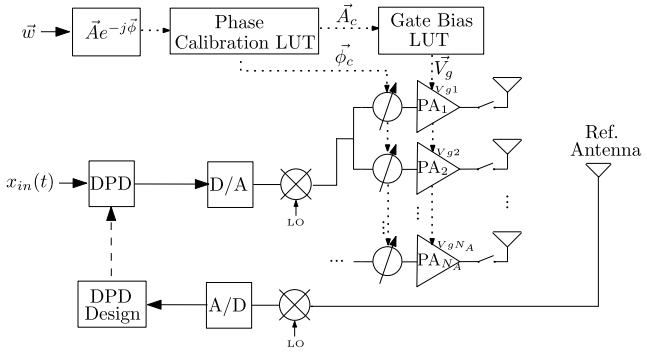

Fig. 14. Gate-bias-controlled beamforming and array DPD.

Also, the total nonlinearity expressed in terms of TRACPR is calculated by integrating it over the space similarly as in [18], [23]. Since we have single-polarized antennas, we ignore the polarization domain. Also, due to the lack of elevation domain beam measurements, the approximated TRP is calculated only over the azimuth domain with 0° elevation angle. However, it is expected that only azimuth domain tapering would not have an impact on the power spread over the elevation domain. Finally, the efficiencies are also calculated with various SLL targets.

A. OTA DPD Training

The measurement setup was presented in Section IV-B. The reference antenna at the main lobe was used as a feedback RX to train the DPD to the beamforming direction. The DPD was trained over 10^5 samples by using the LS method. The DPD training was performed after the bias calibration with all TX paths active. The DPD model was a memory polynomial with nonlinearity up to 9th order and memory length of 5. The polynomial contained only odd-order nonlinearities and hence the number of coefficients was 25. All the other measurement parameters are equal to the measurements presented in Section IV-B.

B. Radiated Linearization Performance

Channel power and ACP results in untapered case are shown in Fig. 15(a) and the corresponding beams in Fig. 16(a). The calculated TRACPRs along with the other figures of merit are collected in Table II. The ACP improvement per PA with OTA trained array DPD is around the same for all PAs. Similarly, the beam of the ACP with and without DPD looks nearly symmetric indicating almost evenly distributed nonlinearity over the PAs. TRACPR was improving 11 dB and EVM was improved from 8.5% without DPD to 4.9% with DPD.

The OTA measurement results with tapered biasing calibration schemes are shown in Fig. 15(b) and (c) and the corresponding beams in Fig. 16(b) and (c). As noticed, the SLLs are low also with DPD, and hence, the DPD does not have a significant impact on the beam shape of the linear part of the signal. The ACP is decreased for all PAs indicating similar nonlinearity per PA. This supports the simulation results presented in Section III-C. Note that ACPR is decreased in all directions. The corresponding TRACPRs are improved from -28.8 and -29.6 dB to -39.9 and -41.6 dB with DPD, which is just around 0.8 dB less than the maximum ACPR measured in the main lobe. The measured EVMs in the main lobe are improved from 8.3% and 8.9% to 4.9% and 4.8% with DPD. The achievable EVM values are limited also by other RF nonidealities, such as IQ-imbalance and phase noise [41]. The measured main-lobe efficiencies are above $\eta_{\text{EIRP}} = 22\%$ and total radiated efficiencies are better than $\eta_{\text{TRP}} = 2.8\%$ with DPD. Note that uniform amplitude is biased for similar main-lobe EIRP than in the tapering scenarios, and hence, the efficiency values given here do not correspond to the performance with maximum EIRP. The main-lobe efficiency η_{EIRP} is around two times higher than in Section III-C due to the fact that, in measurements, we have two times more antennas (two eight-element rows). Hence, the results are well in line with Section III-C.

C. Sidelobe Reduction Performance and Efficiency of Bias Tapering

In order to further verify the limits of the sidelobe reduction performance by bias tapering and its impact on the array linearization, we swept the target SLL of the Taylor tapering. The SLL target was swept from -20 to -30 dB with 1-dB steps. Similarly, as in Section V-B, the array is linearized by common DPD by using the reference antenna. The measured EIRPs, achieved SLLs, and efficiencies with and without DPD are shown in Fig. 17. When the SLL target is reduced, also the achieved EIRP is slightly reduced, as shown in Fig. 17(a). This is due to the fact that for the higher SLL target, the Taylor window has more power dynamics between the lowest and highest driven PAs. Hence, as the power of the center PAs is kept fixed and the power of the side PAs is reduced, the overall EIRP is slightly decreasing. DPD is having only small impact on the EIRP. The achieved SLLs are shown in Fig. 17(b). Similarly, as in the example with -24-dB tapering given in earlier, the right SLL is higher mainly due to the differences in antenna elements and errors in phase and amplitude. The performance drop of the left SLL is around $2-4$ dB with respect to the target SLL. In the best measured case, the measured sidelobes were -26.5 and -23.5 dB on the left and right sides, respectively. It is expected that with more accurate PSs, better SLLs could be achieved. Hence, nonlinear AMPM and its impact on the tapering via traditional input power control as well as bias tapering limits the sidelobe reduction performance and sets calibration requirements for PSs if the SLL is desired to be maintained across various steering angles in different scenarios.

The achieved efficiencies are shown in Fig. 17(c). η_{EIRP} follows the EIRP behavior, i.e., for higher EIRPs, also the efficiency is higher. However, η_{TRP} remains nearly constant due to the fact that the overall array power is not significantly reducing, while the power consumption is constant. Note that these efficiencies are measured with modulated signals and hence under significant backoff. For further improving the efficiency and balance between the total linearization

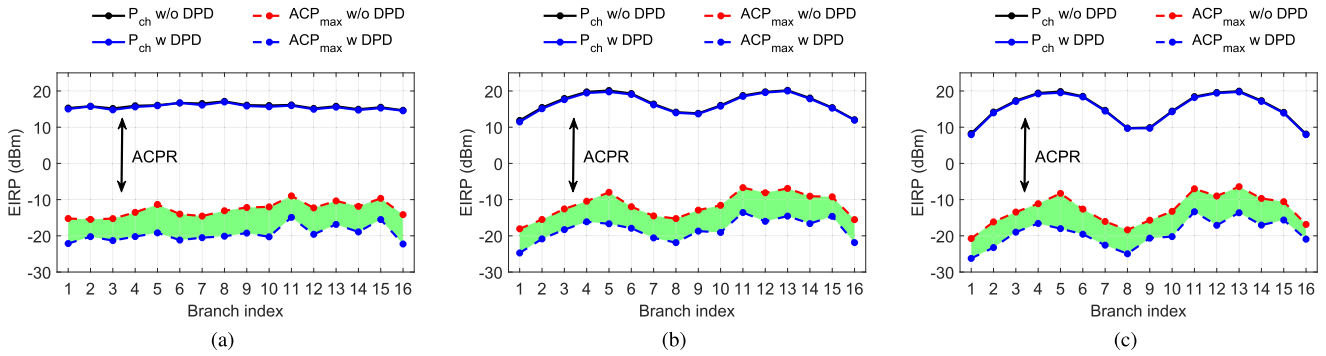

Fig. 15. OTA-measured P_{ch} and ACP_{max} per branch with and without DPD for for (a) uniform amplitude excitation, (b) −24-dB, and (c) −30-dB Taylor tapering PA bias calibration. In the figures, the green area indicates the ACP improvement of DPD for each PA.

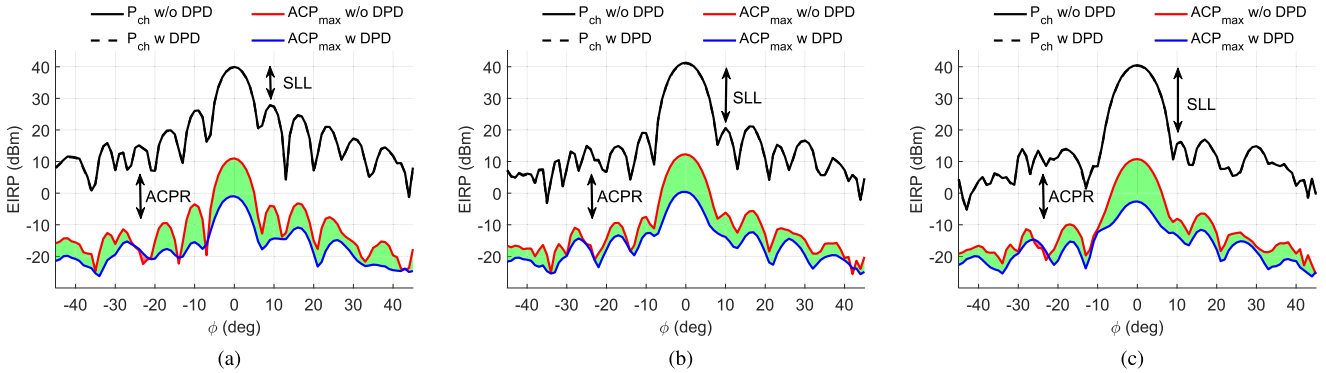

Fig. 16. OTA-measured beams of P_{ch} and ACP_{max} with and without DPD for for (a) uniform amplitude excitation, (b) −24-dB, and (c) −30-dB Taylor tapering PA bias calibration. In the figures, the green area indicates the ACP improvement of DPD in different directions.

TABLE II

MEASURED EIRP, MAIN-LOBE ACPR, TRACPR, EVM, EFFICIENCY, AND SLL FOR DIFFERENT PA BIASING TARGETS WITH AND WITHOUT DPD. *SIDELOBES AND ACPRS ARE PRESENTED AS LEFT/RIGHT

Scenario	EIRP (dBm)	SLL* (dB)	EVM (%)	ACPR* (dB)	TRACPR* (dB)	η_{EIRP} (%)	η_{TRP} (%)
Uniform w/o DPD	39.9	-13.8 / -12.1	8.5	-28.9 / -36.4	-28.8 / -36.1	20.1	2.3
Uniform w DPD	39.8	-13.8 / -12.0	4.9	-40.8 / -46.0	-39.8 / -44.4	19.4	2.2
−24 dB Taylor taper w/o DPD	41.2	-22.2 / -20.2	8.3	-29.0 / -37.3	-28.8 / -37.0	24.8	2.9
−24 dB Taylor taper w DPD	41.1	-22.2 / -20.2	4.9	-40.7 / -46.4	-39.9 / -44.5	23.7	2.8
−30 dB Taylor taper w/o DPD	40.5	-26.4 / -23.5	8.9	-29.7 / -34.1	-29.6 / -34.1	22.9	2.9
−30 dB Taylor taper w DPD	40.4	-26.4 / -23.4	4.8	-42.9 / -46.8	-41.6 / -44.3	22.3	2.8

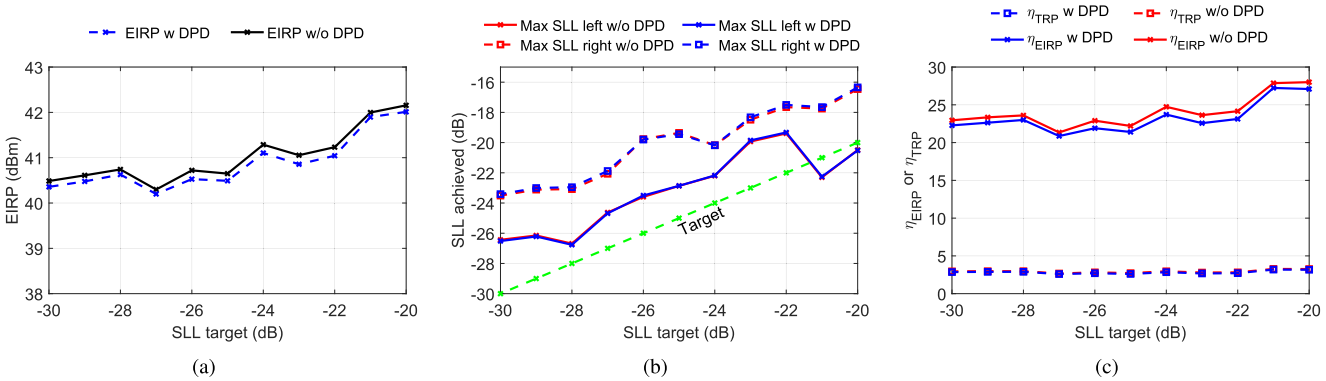

Fig. 17. Measured (a) EIRPs, (b) sidelobe reduction performance, and (c) efficiencies versus the SLL target for Taylor taper PA bias calibration.

performance, EVM, efficiency, and power, the optimal case would be to tune both the input amplitudes and the individual PA bias points.

The measured EVM and TRACPR are given in Fig. 18. With all SLL targets, the EVM is reducing to around 5% and TRACPR is reducing to better than 40 dB.

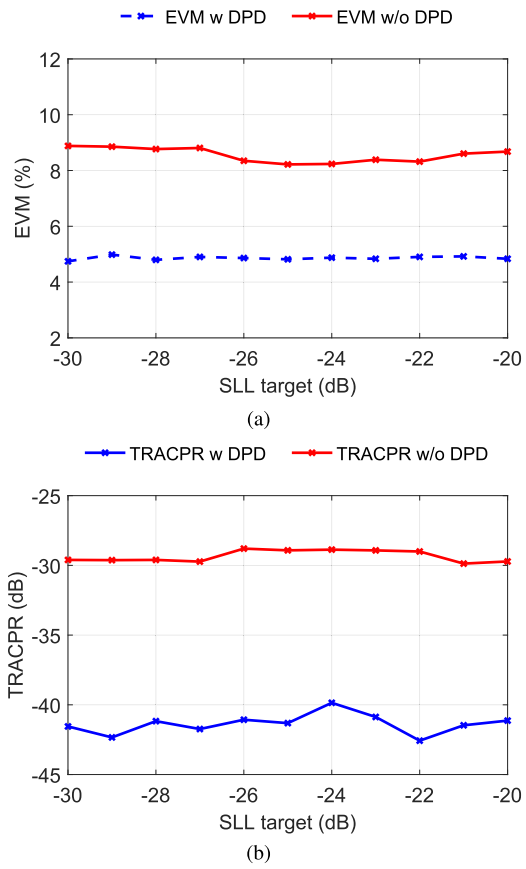

Fig. 18. Measured (a) EVMs and (b) TRACPRs versus the SLL target of Taylor taper PA bias calibration.

Hence, the presented concept works also with higher SLL targets and bias tapered arrays can be linearized by a single DPD to achieve good EVM, SLL, and TRACPR simultaneously.

VI. Conclusion

Linearity and efficiency are important figures of merit to improve in order to enable the widespread usage of mmW beamforming arrays in 5G and future 6G systems. However, combining the traditional DPD and beamforming concepts is challenging due to the shared digital input of multiple elements and per-branch amplitude control used to shape the beam patterns. This article presented an efficient amplitude control scheme of the phased array TX where the per-branch amplitude was controlled only by PA biasing instead of traditional input amplitude control. The gate voltages are synthesized to produce the Taylor window at the PA outputs to reduce the SLL. Due to the nonlinear impact of the PA bias control, the main focus was to show that the impact on the overall radiated nonlinearity can be efficiently improved by array DPD if the bias is able to control the PAs to have a similar shape of nonlinearity. The concept was studied by simulations comparing the presented approach with the traditional approach where the amplitude is controlled before the PAs. Especially, due to the nonlinear AMPM, the good SLL was achieved over different power levels of the input signal, while the DPD performance was excellent over the angular domain.

The concept was validated by the OTA measurements with 16-path phased array TX operating at the 28.1-GHz center frequency. The OTA measurements were performed with 100-MHz-wide 64-QAM CP-OFDM waveform by measuring the beam pattern of the channel power and ACP. Furthermore, main-lobe EVM, efficiencies, and TRACPR were measured. In the best scenario, the bias tapering showed a −23.5-dB maximum SLL with 4.8% main-lobe EVM and −41.6-dB TRACPR. Across all measured configurations, −40-dB TRACPR and 5% EVM were achieved.

The presented concept gives a new approach to control both the beam pattern and the linearity in phased array TXs. PA biasing gives systematic control for the per-PA nonlinearity that can be used for beamforming the distortion. However, the presented approach requires that the PA array has to be calibrated for different PA bias voltages, which requires power and phase detectors or feedback paths for each PA. Alternatively, OTA reference antennas can also be used for systematic PA calibration. On the other hand, the DPD approach can be simplified if the nonlinearity of all PAs can be made more similar. The complexity of the feedback RX and DPD can be decreased to measure only one or just a few PAs for training the DPD. The bias control can use the same biasing DACs that are used in bias-up and bias-down procedures as well as adaptive temperature compensation. Similarly, the same feedback RX used for DPD can be used for calibrating the powers and phases with different bias points. Hence, the presented approach as such does not increase the hardware complexity compared to the systems that already have the means to bias the PAs, calibrate phase and amplitudes, and perform DPD by using a feedback RX.

Acknowledgment

The authors would like to thank Keysight Technologies for laboratory equipment and fifth-generation new radio (5GNR) waveform support.

References

[1] M. Latva-Aho and K. Leppänen, *Key Drivers and Research Challenges for 6G Ubiquitous Wireless Intelligence*. Oulu, Finland: Univ. Oulu, Sep. 2019.

[2] X. Liu *et al.*, "Beam-oriented digital predistortion for 5G massive MIMO hybrid beamforming transmitters," *IEEE Trans. Microw. Theory Techn.*, vol. 66, no. 7, pp. 3419–3432, Jul. 2018.

[3] N. Tervo *et al.*, "Digital predistortion concepts for linearization of mmW phased array transmitters," in *Proc. 16th Int. Symp. Wireless Commun. Syst. (ISWCS)*, Aug. 2019, pp. 325–329.

[4] E. Ng, Y. Beltagy, G. Scarlato, A. Ben Ayed, P. Mitran, and S. Boumaiza, "Digital predistortion of millimeter-wave RF beamforming arrays using low number of steering angle-dependent coefficient sets," *IEEE Trans. Microw. Theory Techn.*, vol. 67, no. 11, pp. 4479–4492, Nov. 2019.

[5] N. Tervo, J. Aikio, T. Tuovinen, T. Rahkonen, and A. Parssinen, "Digital predistortion of amplitude varying phased array utilising over-the-air combining," in *IEEE MTT-S Int. Microw. Symp. Dig.*, Jun. 2017, pp. 1165–1168.

[6] *NR Base Station (BS) Radio Transmission and Reception*, Standard 3GPP Tech. Spec. 38.104-2, v16.3.0 (Release 16), Mar. 2020.

[7] *NR; Base Station (BS) Conformance Testing Part 2: Radiated Conformance Testing*, Standard 3GPP Tech. Spec. 38.141-2, v16.3.0 (Release 16), Mar. 2020.

[8] S. Lee *et al.*, "Digital predistortion for power amplifiers in hybrid MIMO systems with antenna subarrays," in *Proc. IEEE 81st Veh. Technol. Conf. (VTC Spring)*, May 2015, pp. 1–5.

[9] X. Liu, W. Chen, L. Chen, F. M. Ghannouchi, and Z. Feng, "Linearization for hybrid beamforming array utilizing embedded over-the-air diversity feedbacks," *IEEE Trans. Microw. Theory Techn.*, vol. 67, no. 12, pp. 5235–5248, Dec. 2019.

[10] R. Murugesu, M. Holyoak, H. Chow, and S. Shahramian, "Linearization of mm-wave large-scale phased arrays using near-field coupling feedback for >10Gb/s wireless communication," in *IEEE MTT-S Int. Microw. Symp. Dig.*, Aug. 2020, pp. 1271–1274.

[11] X. Wang, C. Yu, Y. Li, W. Hong, and A. Zhu, "Real-time single channel over-the-air data acquisition for digital predistortion of 5G massive MIMO wireless transmitters," in *IEEE MTT-S Int. Microw. Symp. Dig.*, May 2019, pp. 1–3.

[12] E. Ng, Y. Beltagy, P. Mitran, and S. Boumaiza, "Single-input single-output digital predistortion of power amplifier arrays in millimeter wave RF beamforming transmitters," in *IEEE MTT-S Int. Microw. Symp. Dig.*, Jun. 2018, pp. 481–484.

[13] W. Pan *et al.*, "Digital linearization of multiple power amplifiers in phased arrays for 5G wireless communications," in *Proc. IEEE Int. Symp. Signal Process. Inf. Technol. (ISSPIT)*, Dec. 2018, pp. 247–251.

[14] X. Wang, Y. Li, C. Yu, W. Hong, and A. Zhu, "Digital predistortion of 5G massive MIMO wireless transmitters based on indirect identification of power amplifier behavior with OTA tests," *IEEE Trans. Microw. Theory Techn.*, vol. 68, no. 1, pp. 316–328, Jan. 2020.

[15] Q. Luo, X.-W. Zhu, C. Yu, and W. Hong, "Single-receiver over-the-air digital predistortion for massive MIMO transmitters with antenna crosstalk," *IEEE Trans. Microw. Theory Techn.*, vol. 68, no. 1, pp. 301–315, Jan. 2020.

[16] N. Tervo, M. E. Leinonen, J. Aikio, T. Rahkonen, and A. Parssinen, "Analyzing the effects of PA variations on the performance of phased array digital predistortion," in *Proc. IEEE 29th Annu. Int. Symp. Pers., Indoor Mobile Radio Commun. (PIMRC)*, Sep. 2018, pp. 215–219.

[17] M. Abdelaziz, L. Anttila, A. Brihuega, F. Tufvesson, and M. Valkama, "Digital predistortion for hybrid MIMO transmitters," *IEEE J. Sel. Topics Signal Process.*, vol. 12, no. 3, pp. 445–454, Jun. 2018.

[18] N. Tervo *et al.*, "Digital predistortion of phased-array transmitter with shared feedback and far-field calibration," *IEEE Trans. Microw. Theory Techn.*, vol. 69, no. 1, pp. 1000–1015, Jan. 2021.

[19] S. Hesami, S. R. Aghdam, C. Fager, T. Eriksson, R. Farrell, and J. Dooley, "Single digital predistortion technique for phased array linearization," in *Proc. IEEE Int. Symp. Circuits Syst. (ISCAS)*, May 2019, pp. 1–5.

[20] C. Fager, K. Hausmair, K. Buisman, K. Andersson, E. Sienkiewicz, and D. Gustafsson, "Analysis of nonlinear distortion in phased array transmitters," in *Proc. Integr. Nonlinear Microw. Millimetre-Wave Circuits Workshop (INMMiC)*, Apr. 2017, pp. 1–4.

[21] K. Hausmair, U. Gustavsson, C. Fager, and T. Eriksson, "Modeling and linearization of multi-antenna transmitters using over-the-air measurements," in *Proc. IEEE Int. Symp. Circuits Syst. (ISCAS)*, May 2018, pp. 1–4.

[22] C. Yu *et al.*, "Full-angle digital predistortion of 5G millimeter-wave massive MIMO transmitters," *IEEE Trans. Microw. Theory Techn.*, vol. 67, no. 7, pp. 2847–2860, Jul. 2019.

[23] A. Brihuega *et al.*, "Piecewise digital predistortion for mmWave active antenna arrays: Algorithms and measurements," *IEEE Trans. Microw. Theory Techn.*, vol. 68, no. 9, pp. 4000–4017, Sep. 2020.

[24] C. Li, S. He, F. You, J. Peng, and P. Hao, "Analog predistorter averaged digital predistortion for power amplifiers in hybrid beamforming multi-input multi-output transmitter," *IEEE Access*, vol. 8, pp. 146145–146153, 2020.

[25] S. Hesami, S. R. Aghdam, J. Dooley, T. Eriksson, and C. Fager, "Amplitude varying phased array linearization," in *Proc. 50th Eur. Microw. Conf. (EuMC)*, Jan. 2021, pp. 348–351.

[26] S. Habu, Y. Yamao, H. Ishikawa, and T. Maniwa, "Outband radiation and modulation accuracy of unified beamforming DPD," in *Proc. IEEE 29th Annu. Int. Symp. Pers., Indoor Mobile Radio Commun. (PIMRC)*, Sep. 2018, pp. 225–230.

[27] C. Fager, T. Eriksson, F. Barradas, K. Hausmair, T. Cunha, and J. C. Pedro, "Linearity and efficiency in 5G transmitters: New techniques for analyzing efficiency, linearity, and linearization in a 5G active antenna transmitter context," *IEEE Microw. Mag.*, vol. 20, no. 5, pp. 35–49, May 2019.

[28] K. Hausmair *et al.*, "Prediction of nonlinear distortion in wideband active antenna arrays," *IEEE Trans. Microw. Theory Techn.*, vol. 65, no. 11, pp. 4550–4563, Nov. 2017.

[29] C. Mollen, E. G. Larsson, U. Gustavsson, T. Eriksson, and R. W. Heath, "Out-of-band radiation from large antenna arrays," *IEEE Commun. Mag.*, vol. 56, no. 4, pp. 196–203, Apr. 2018.

[30] E. G. Larsson and L. Van Der Perre, "Out-of-band radiation from antenna arrays clarified," *IEEE Wireless Commun. Lett.*, vol. 7, no. 4, pp. 610–613, Aug. 2018.

[31] L. Anttila, A. Brihuega, and M. Valkama, "On antenna array out-of-band emissions," *IEEE Wireless Commun. Lett.*, vol. 8, no. 6, pp. 1653–1656, Dec. 2019.

[32] O. Kursu *et al.*, "Design and measurement of a 5G mmW mobile backhaul transceiver at 28 GHz," *EURASIP J. Wireless Commun. Netw.*, vol. 2018, no. 1, p. 201, Aug. 2018.

[33] M. Jokinen, O. Kursu, N. Tervo, J. Saloranta, M. E. Leinonen, and A. Parssinen, "Over-the-air phase measurement and calibration method for 5G mmW phased array radio transceiver," in *Proc. 93rd ARFTG Microw. Meas. Conf. (ARFTG)*, Jun. 2019, pp. 1–4.

[34] T. Rahkonen, S. Hietakangas, and J. Aikio, "AM-PM distortion caused by transistor's signal-dependent input impedance," in *Proc. 20th Eur. Conf. Circuit Theory Design (ECCTD)*, Aug. 2011, pp. 833–836.

[35] N. Chugh, M. Bhattacharya, M. Kumar, and R. S. Gupta, "Impact of donor layer thickness, doping concentration and gate-width on gate-capacitance of AlGaN/GaN single and double heterostructure HEMT for microwave frequency applications," in *Proc. IEEE Electron Devices Kolkata Conf. (EDKCON)*, Nov. 2018, pp. 207–212.

[36] B. Sadhu *et al.*, "A 28-GHz 32-element TRX phased-array IC with concurrent dual-polarized operation and orthogonal phase and gain control for 5G communications," *IEEE J. Solid-State Circuits*, vol. 52, no. 12, pp. 3373–3391, Dec. 2017.

[37] R. Hansen, *Phased Array Antennas*, vol. 14. Hoboken, NJ, USA: Wiley, 1998.

[38] T. A. Hill and J. R. Kelly, "28 GHz Taylor feed network for sidelobe level reduction in 5G phased array antennas," *Microw. Opt. Technol. Lett.*, vol. 61, no. 1, pp. 37–43, Jan. 2019.

[39] M. E. Leinonen, G. Destino, O. Kursu, M. Sonkki, and A. Pärssinen, "28 GHz wireless backhaul transceiver characterization and radio link budget," *ETRI J.*, vol. 40, no. 1, pp. 89–100, Feb. 2018.

[40] M. Sonkki *et al.*, "Linearly polarized 64-element antenna array for mm-wave mobile backhaul application," in *Proc. 12th Eur. Conf. Antennas Propag. (EuCAP)*, Apr. 2018, pp. 1–5.

[41] M. E. Leinonen, M. Jokinen, N. Tervo, O. Kursu, and A. Parssinen, "System EVM characterization and coverage area estimation of 5G directive mmW links," *IEEE Trans. Microw. Theory Techn.*, vol. 67, no. 12, pp. 5282–5295, Dec. 2019.

Nuutti Tervo (Graduate Student Member, IEEE) received the B.Sc. (Tech.) and M.Sc. (Tech.) degrees in electrical engineering from the University of Oulu, Oulu, Finland, in 2014, where he is currently pursuing the Ph.D. degree at the Centre for Wireless Communications (CWC). His Ph.D. dissertation research focuses on nonlinearity and linearization of millimeter-wave beamforming transceivers.

He has a strong background in different fields of wireless communications, including radio frequency (RF), radio channel modeling, signal processing, and system-level analysis. Around those topics, he has already authored or coauthored more than 45 international journal articles and conference papers. He holds patents.

Mr. Tervo was a recipient of the Young Scientist Award of the URSI XXXV Finnish Convention on Radio Science, Tampere, in 2019.

Bilal Khan (Graduate Student Member, IEEE) received the B.Sc. degree in electrical engineering (communication) from the University of Engineering and Technology Peshawar, Peshawar, Pakistan, in 2013, and the M.Sc. degree in wireless communication engineering from the University of Oulu, Oulu, Finland, in 2016, where he is currently pursuing the Ph.D. degree.

His research interest includes digital predistortion for radio frequency (RF) power amplifiers with an emphasis on robust and simplified linearization solutions for multiantenna transmitters in millimeter-wave systems.

Janne P. Aikio was born in Haukipudas, Finland, in 1977. He received the M.Sc. and Ph.D. degrees in electrical engineering from the University of Oulu, Oulu, Finland, in 2002 and 2007, respectively.

He is currently a Post-Doctoral Researcher with the University of Oulu. His technical interests lie in the fields of millimeter-wave integrated power amplifiers and modeling and analysis of distortion of radio frequency (RF) power amplifiers.

Olli Kursu received the M.Sc. and Ph.D. degrees in electrical and electronics engineering from the University of Oulu, Oulu, Finland, in 2006 and 2015, respectively.

He is currently working as a Post-Doctoral Researcher at the Centre for Wireless Communications, University of Oulu. His research interests include millimeter-wave (mmW), radio frequency (RF), analog, and mixed-signal circuit design for wireless communication systems.

Markku Jokinen received the M.Sc. degree in electronics from the University of Oulu, Oulu, Finland, in 2010, where he is currently pursuing the Ph.D. degree with a focus on measurement techniques.

He is currently working as a Research Scientist at the Centre for Wireless Communications, University of Oulu. He has gained experience in the design and implementation of wireless system algorithms and protocols with software-defined radio platforms.

Marko E. Leinonen (Member, IEEE) received the M.Sc., Lic., and Doctor of Science degrees in electrical engineering from the University of Oulu, Oulu, Finland, in 1996, 2002, and 2020, respectively.

From 1994 to 2012, he was with Nokia Mobile Phones, Oulu, where he worked in various positions with radio engineering and technology management. From 2006 to 2007, he was a Senior Engineering Manager in Bengaluru, India. From 2012 to 2016, he was a Master Developer with Ericsson, Oulu. Since 2017, he has been with the Centre for Wireless Communications, University of Oulu, where he is currently the Research Manager. He holds 40 granted international patent families concentrating on radio engineering. His research interests include wireless radio systems and quality topics in radio engineering.

Marko Sonkki (Senior Member, IEEE) received the M.Sc. degree in electrical engineering and the Doctoral of Science degree (D.Sc.) degree in radio telecommunications engineering from the University of Oulu, Oulu, Finland, in 2004 and 2013, respectively. The master's thesis was related to a measurement transmitter for adaptive antennas. The topic of the dissertation was wideband and multielement antennas for wireless applications, which was focusing on antenna design based on spherical and characteristic modes theories.

He is currently working in the private sector and doing cooperation as a Post-Doctoral Researcher with the Centre for Wireless Communications (CWC), Faculty of Information Technology and Electrical Engineering (ITEE), University of Oulu. His current research interests are the design and analysis of wideband antennas, wideband multimode and full-duplex antennas, and antenna arrays, including millimeter waves.

Timo Rahkonen (Member, IEEE) was born in Jyvaskylä, Finland, 1962. He received the Diploma, Licentiate, and Doctor of Technology degrees from the University of Oulu, Oulu, Finland, in 1986, 1991, and 1994, respectively.

He is currently a Professor in circuit theory and circuit design at the University of Oulu, where he is conducting research on linearization and error correction techniques for radio frequency (RF) power amplifiers and A/D and D/A converters.

Aarno Pärssinen (Senior Member, IEEE) received the M.Sc., Licentiate in Technology, and Doctor of Science degrees in electrical engineering from the Helsinki University of Technology, Helsinki, Finland, in 1995, 1997, and 2000, respectively.

From 1994 to 2000, he was with the Electronic Circuit Design Laboratory, Helsinki University of Technology, working on direct conversion RXs and subsampling mixers for wireless communications. In 1996, he was a Research Visitor at the University of California at Santa Barbara, Santa Barbara, CA, USA. From 2000 to 2011, he was with the Nokia Research Center, Helsinki. From 2011 to 2013, he was at Renesas Mobile Corporation, Helsinki, as a Distinguished Researcher and the RF Research Manager. From October 2013 to September 2014, he was an Associate Technical Director at Broadcom, Helsinki. Since September 2014, he has been with the Centre for Wireless Communications, University of Oulu, Oulu, Finland, where he is currently a Professor. He is leading the devices and circuits research area in the 6G flagship program financed by the Academy of Finland. He is one of the original contributors to Bluetooth low energy extension, now called BT LE. He has authored or coauthored one book, two book chapters, and more than 150 international journal articles and conference papers. He holds several patents. His research interests include wireless systems and transceiver architectures for wireless communications with special emphasis on radio frequency (RF) and analog integrated circuit and system design.

Dr. Pärssinen served as a member of the Technical Program Committee of the International Solid-State Circuits Conference from 2007 to 2017, where he was the Chair of the European Regional Committee from 2012 to 2013 and the Wireless Sub-Committee from 2014 to 2017. From 2009 to 2011, he served as a member for the Nokia CEO Technology Council. He has served as a Solid-State Circuits Society Representative for the IEEE 5G Initiative from 2015 to 2019.